Electronic structure of disordered Nb - Mo alloys studied using the charge-self-consistent Korringa - Kohn - Rostoker coherent potential approximation

1996 J. Phys.: Condens. Matter 8 2929

(http://iopscience.iop.org/0953-8984/8/17/006)

J. Phys.: Condens. Matter **8** (1996) 2929–2944. Printed in the UK

Electronic structure of disordered Nb–Mo alloys studied using the charge-self-consistent Korringa–Kohn–Rostoker coherent potential approximation

S S Rajput†§, R Prasad†, R M Singru†, S Kaprzyk‡‖ and A Bansil‡

† Department of Physics, Indian Institute of Technology, Kanpur, 208016, India

‡ Department of Physics, Northeastern University, Boston, MA 02115, USA

Received 19 December 1995

Abstract. We present an all-electron fully charge-self-consistent Korringa–Kohn–Rostoker coherent potential approximation (KKR-CPA) study of the electronic structures of disordered bcc $Nb_{1-x}Mo_x$ alloys over the entire composition range. Specific computations are reported for x = 0.0, 0.25, 0.50, 0.75, and 1.0. Extensive comparisons with the predictions of the Nb-based rigid-band model (RBM) and other theoretical results, as well as with the relevant experimental results insofar as they are available are made. The particular issues that we focus on concern the evolution of the Fermi surface (FS), and the changes in the density of states and the superconducting transition temperature (T_c) of Nb with increasing Mo content. The N- and H-centred FS sheets of Nb are found to shrink essentially rigidly, but the Γ-centred sheets evolve in a highly non-rigid-band manner. The $x = 0.25$ Mo alloy displays an especially large disorder-induced smearing of the Γ-centred FS sheets. Direct experimental information concerning the FS is available only for the N-centred sheet via positron annihilation and in this regard our results are in accord with the measurements. Concerning superconductivity, we have computed the Hopfield parameters η_{Nb} and η_{Mo} for the Nb and Mo sites, and used the results to obtain T_c for $Nb_{1-x}Mo_x$ via the McMillan formula. We find that this simple scheme describes the observed composition dependence of T_c in $Nb_{1-x}Mo_x$ reasonably well.

1. Introduction

The electronic structure and properties of disordered alloys have attracted considerable interest in recent years. Although many theoretical approaches have been proposed in this connection, it is generally agreed now that the Korringa–Kohn–Rostoker coherent potential approximation (KKR-CPA) is the best single-site scheme for treating random substitutional alloys (see [1–5], and references therein). The KKR-CPA combined with the density functional method, as practised currently, constitutes a parameter-free theory of alloys of a sophistication comparable to the band theory of pure materials.

Of specific interest to this article is the Nb–Mo transition–transition metal system, which is one of the most extensively studied, experimentally as well as theoretically, among the group VB–VIB constituents [6–28]. Motivation for this has been severalfold. Nb possesses the highest superconducting transition temperature (T_c) among elemental metals. The average number of electrons per atom can be varied continuously in $Nb_{1-x}Mo_x$ since

§ Permanent address: Bundelkhand Institute of Engineering and Technology, Jhansi, 284001, India.

‖ Permanent address: Academy of Mining and Metallurgy, Institute of Physics and Nuclear Techniques, Krakow, Poland.

0953-8984/96/172929+16$19.50

it forms a bcc solid solution for all x [6]. These alloys remain superconducting throughout the composition range, the T_c decreasing from 9.25 K in Nb to 0.9 K in Mo [7–15]. Nb and Mo both possess partially filled 4d shells and have very similar band structures [16, 17] indicating the alloys to be in the weak-scattering regime [12]. However, the Fermi surfaces (FSs) of Nb and Mo differ substantially [16, 17] due to different electron counts, and, consequently, the FS topology of the alloy changes quite drastically with composition. It is clear then that Nb–Mo alloys constitute a system of great physical interest for testing and developing models of electron–phonon interaction and superconductivity, of disorder effects, and of the interplay between FS topology and changes in various physical properties of alloys.

Here we present highly precise all-electron fully charge-self-consistent KKR-CPA results for $Nb_{1-x}Mo_x$ over the entire composition range, including pure Nb and Mo limits, all computations having been carried out within very similar frameworks. Many computations on Nb–Mo alloys within the virtual-crystal approximation (VCA), the average t-matrix approximation (ATA), as well as the CPA have been reported in the literature, including a discussion of the Compton, positron annihilation 2D angular correlation (2D-ACAR), and soft x-ray spectra, and the superconducting properties [18–27]. All of the previous computations are however non-self-consistent, being based on a variety of prescriptions for obtaining the crystal potential; to our knowledge, full charge self-consistency has not been achieved in any of the earlier work on the Nb–Mo system. In contrast, the present results, being fully self-consistent, constitute unique predictions of the theory, and provide a more satisfactory testbed for confronting the underlying one-electron picture with experiment.

Table 1. Theoretical and experimental radii of various Fermi surface sheets along representative high-symmetry directions in Nb, expressed as fractions of the distance between the symmetry points Γ and H in the Nb Brillouin zone.

Sheet	Direction	Experiment [35]	Theory 1 [36]	Theory 2 [27]	Theory 3 [16]	Present theory
Γ-centred	Γ to H	0.39	0.40	0.38	0.37	0.380
octahedron	Γ to N	0.19	0.17	0.17	0.14	0.155
(GCO)	Γ to P	—	—	—	0.16	0.171
N-centred	N to Γ	0.30	0.32	0.32	0.34	0.313
ellipsoid	N to H	0.20	0.19	0.19	0.20	0.192
(NCE)	N to P	—	—	—	0.32	0.323
'Jungle-gym'	N to Γ	0.41	0.41	0.43	0.40	0.447
(JGA)	N to H	0.28	0.29	0.29	0.27	0.286
	Γ to P	—	—	—	0.16	0.171

We focus on the evolution of the FS of $Nb_{1-x}Mo_x$ and present, for the first time to our knowledge, changes in the shapes and radii of various FS sheets in quantitative detail, whereas much of the existing literature [18–23] in this regard is rather qualitative. The nature of electronic states at the Fermi energy is delineated clearly. In connection with the superconductivity of $Nb_{1-x}Mo_x$, we have used the computed electronic structure to obtain the electron–phonon coupling constants (λs) as a function of x in terms of the Hopfield parameters (ηs). The use of this estimate of λs in the McMillan formula [11], together with the expression for μ^* given by Bennemann and Garland [29], yields a composition dependence of T_c in $Nb_{1-x}Mo_x$ which is in reasonable accord with the measurements.

Relatively little experimental literature is available on Nb–Mo alloys by way of direct

measurements of the FS dimensions. We note the positron annihilation (2D-ACAR) measurements of Bull *et al* (see [26, 27]) on $Nb_{0.5}Mo_{0.5}$, and a more limited 2D-ACAR study by Manuel *et al* [24] on $Nb_{0.75}Mo_{0.25}$ single crystals. Powell *et al* [14] have measured several branches of phonon dispersion curves in Nb, Mo, and Nb–Mo alloys, and observed a number of Kohn anomalies whose location gives some information, albeit indirect, concerning the FSs. In connection with superconductivity, the composition dependence of λ and T_c in Nb–Mo is reported in [11] and [15]. A note may also be made of the thermomodulation and soft x-ray studies [19, 20], and of the temperature coefficient of the elastic shear constant, C_{44}, and the Grüneisen parameter [28]. The latter work shows that the elastic constants behave anomalously in $Nb_{1-x}Mo_x$ around $x = 0.4$, and provides an interesting example of effects that can arise from the interplay between changes in the electron–phonon interactions and the FS topology in alloys.

An outline of this article is as follows. The introductory remarks are followed in section 2 by a brief presentation of computational details. Section 3 turns to a discussion of our results; the FSs, the density of states (DOS), and the superconducting properties are considered in subsections 3.1, 3.2, and 3.3 respectively. We compare and contrast our theoretical predictions with the earlier work, and make contact with experiment as far as possible. Some concluding remarks are made in section 4.

Table 2. As table 1 but for Mo.

Sheet	Direction	Experiment 1 [37]	Experiment 2 [38]	Theory 1 [39]	Theory 2 [27]	Theory 3 [17]	Present theory
Γ-centred	Γ to H	0.57	0.55	0.59	0.58	0.60	0.584
electron 'jack'	Γ to N	0.26	—	0.27	0.26	0.19	0.262
(GCE)	Γ to P	—	—	—	—	0.19	0.236
H-centred	H to Γ	0.40	0.41	0.41	0.42	0.39	0.416
octahedron	H to N	0.30	0.31	0.28	0.30	0.21	0.303
(HCO)							
N-centred	N to Γ	0.16	0.17	0.20	0.19	0.15	0.188
ellipsoid	N to H	0.11	0.11	0.14	0.11	0.09	0.107
(NCE)	N to P	—	—	—	—	0.20	0.195
'Lens'	Diameter along Δ	0.10	—	0.10	0.14	0.15	0.148

2. Computational procedures

The electronic structures of Nb, Mo and disordered $Nb_{1-x}Mo_x$ for x = 0.25, 0.50, and 0.75 were calculated using the all-electron fully charge-self-consistent KKR-CPA methodology [1–5]. Here we limit ourselves to mentioning a few salient features of the KKR-CPA approach, and ask the reader to refer to our earlier work for specific details of our formulation, and of methods for obtaining Fermi surface parameters, densities of states, and related physical quantities [1, 3–5]. Briefly, combining the KKR-CPA with the local density approximation (LDA), which is the common current practice, provides a first-principles, parameter-free mean-field theory for treating electronic structure of a disordered alloy. Insofar as the average properties are concerned, the KKR-CPA replaces the disordered system by a suitably chosen translationally invariant effective medium. Although the periodicity is in some sense thus restored, we emphasize that Bloch states are no longer

eigenstates of the system, but become broadened to reflect the disorder-induced scattering of states; for this reason the FS also becomes blurred or smeared in the alloy. Finally, we note that KKR-CPA computations involve self-consistency at two physically distinct though numerically coupled levels—namely, the determination of the self-consistent CPA medium to incorporate disorder effects, and the calculation of crystal potential which involves the treatment of Coulomb self-consistency within the LDA.

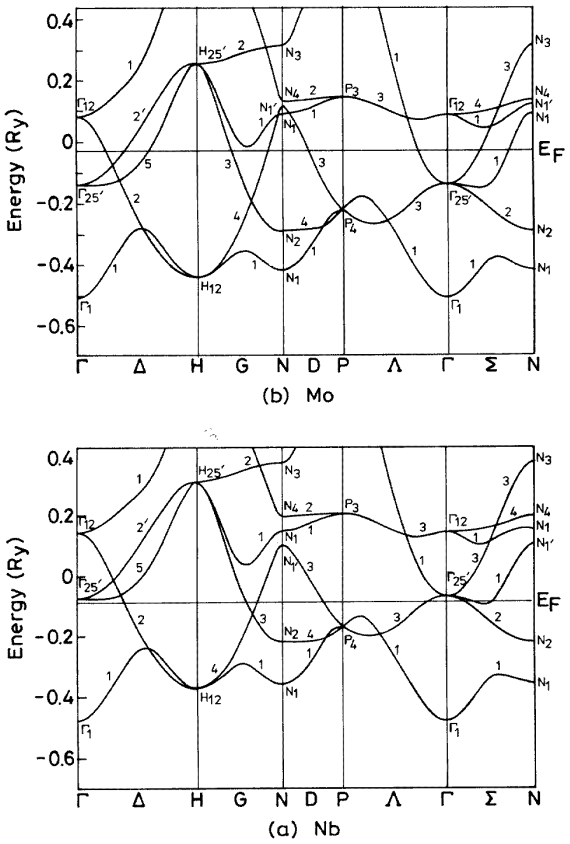

Figure 1. Energy bands for (a) Nb and (b) Mo (after [16] and [17]).

In the present calculations we have used the von Barth–Hedin exchange–correlation potential [30]. Aside from the atomic numbers of Nb ($Z = 41$) and Mo ($Z = 42$), the only input parameters are the lattice constants a; the specific values used are (in atomic units): $a = 6.200$, 6.155, 6.054, 6.015, 5.949 for $x = 0$, 0.25, 0.50, 0.75, 1.0, respectively. The KKR-CPA self-consistent equations were solved to a high degree of accuracy over the whole energy range for each composition; the crystal potentials on Nb and Mo sites were converged to about 1 mRyd in all cases.

Concerning the superconducting properties discussed in section 3.3 below, the value of T_c is computed using the McMillan formula [11]

$$T_c = \frac{\Theta_D}{1.45} \exp\left[\frac{-1.04(1+\lambda)}{\lambda - \mu^*(1+0.62\lambda)}\right] \tag{1}$$

where Θ_D is the Debye temperature and μ^* is the so-called Coulomb pseudopotential

parameter. The prefactor $\Theta_D/1.45$ in equation (1) is accurate for $\lambda \leqslant 1.5$ although the form $\langle\omega_{log}\rangle/1.2$ where $\langle\omega_{log}\rangle$ is the average phonon frequency is suggested by [31] to be preferable.

There is some ambiguity regarding the proper value of μ^*. McMillan [11] suggests a value of 0.13 for Nb–Mo alloys independent of composition, while Papaconstantopoulos *et al* [13] use for a number of metals the following formula given by Bennemann and Garland [29]:

$$\mu^* = \frac{0.26\rho(E_F)}{1+\rho(E_F)}. \tag{2}$$

Here $\rho(E_F)$ is the DOS at the Fermi level E_F in units of states eV^{-1}/atom. There is also the question of renormalization of μ^* as well as λ by the effect of spin fluctuations [32].

The electron–phonon coupling constant λ in equation (1) is calculated by using the formula [33]

$$\lambda = \frac{(1-x)\eta_{Nb}}{M_{Nb}\langle\omega^2\rangle_{Nb}} + \frac{x\eta_{Mo}}{M_{Mo}\langle\omega^2\rangle_{Mo}} \tag{3}$$

where M and $\langle\omega^2\rangle$ denote atomic mass and averaged phonon frequency squared respectively. The ηs are the Nb and Mo site-projected Hopfield parameters calculated within the rigid muffin-tin approximation (RMTA) by using the expression [34]

$$\eta = \sum_l \frac{(2l+2)\rho_l(E_F)\rho_{l+1}(E_F)}{(2l+1)(2l+3)\rho(E_F)} \left| \int_0^{r_{WS}} \mathrm{d}r\ r^2 R_l(r) \frac{\mathrm{d}V}{\mathrm{d}r} R_{l+1}(r) \right|^2 \tag{4}$$

where $V(r)$ is the self-consistent KKR-CPA muffin-tin potential on an Nb or Mo site extending to the Wigner–Seitz sphere of radius r_{WS}, R_l are regular solutions of the Schrödinger equation normalized to unity in the Wigner–Seitz sphere, and ρ_l is the lth partial DOS on the site considered. The obvious superscript Nb (Mo) on various quantities in equation (4) is suppressed for simplicity of notation. We emphasize that great care must be taken in evaluating η via equation (4) since the DOS varies rapidly with energy especially in the Nb-rich alloys. For this reason, we calculated the Fermi energy in all cases to an accuracy of better than 0.1 mRyd, and made extensive tests in order to establish the accuracy of our numerical procedures. Our final value of $\eta_{Nb} = 8.140$ eV Å^{-2} is in reasonable accord with values of 7.627 eV Å^{-2} and 7.069 eV Å^{-2} quoted in [13] and [7] respectively.

3. Results and discussion

3.1. The Fermi surface

Before discussing the FS of $Nb_{1-x}Mo_x$, we recapitulate the FS topology of Nb and Mo with the help of figures 1, 2(a), and 2(e), and tables 1 and 2 [16–28, 35–39]. The FS of Nb, figure 2(a), consists of three sheets: (i) the second-band (the 5s Γ_1 level being numbered as the first band) octahedral hole centred at Γ (GCO); (ii) the third-band distorted ellipsoidal hole centred at N (NCE); and (iii) the third-band multiply connected hole—the so-called jungle-gym arm (JGA), along the $\langle 100\rangle$ directions. The FS of Mo, figure 2(e), consists of four sheets: (i) the fourth-band electron jack centred at Γ (GCE); (ii) the third-band octahedral hole pocket centred at H (HCO); (iii) the third-band ellipsoidal hole pocket centred at the point N (NCE); and (iv) the fifth-band thin electron lenses lying along the ΓH symmetry line. The comparisons of tables 1 and 2 show that our computed FS dimensions in Nb as well as Mo are in excellent accord with existing theoretical and experimental work,

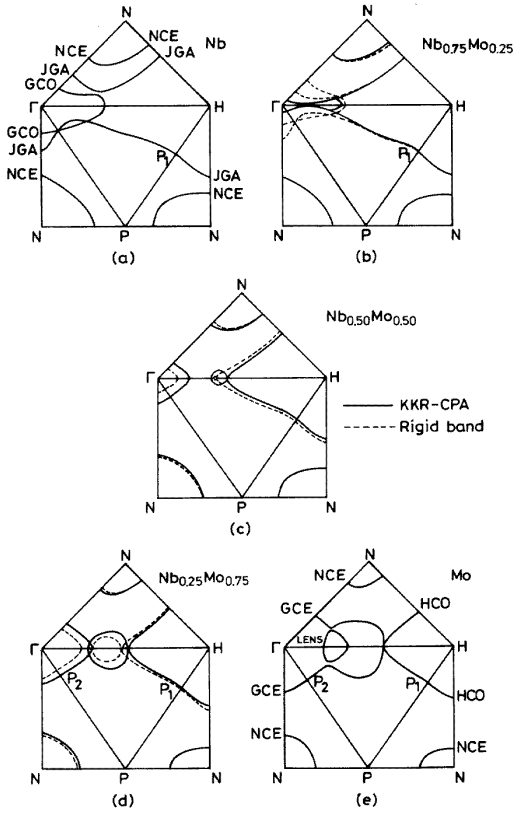

Figure 2. KKR-CPA cross sections of the Fermi surface in (100) and (110) planes: (a) Nb, (b) $Nb_{0.75}Mo_{0.25}$, (c) $Nb_{0.5}Mo_{0.5}$, (d) $Nb_{0.25}Mo_{0.75}$, and (e) Mo. The dashed lines depict the RBM results. The letters P_1 and P_2 denote points which identify flat portions of the FS discussed in the text. The disorder smearing of the FSs of alloys is not shown.

minor differences notwithstanding. Thus in these limiting cases our computations correctly reproduce the electronic structures and the FSs.

Notably, the band structures of Nb and Mo are quite similar as seen by comparing figures 1(a) and 1(b). Despite this, the associated FSs differ substantially; Nb possesses only hole-like sheets, whereas Mo contains two hole-like and two electron-like sheets. These differences originate from the fact that in Nb E_F lies just below $\Gamma_{25'}$ by 17 mRyd, but in Mo E_F moves to 107 mRyd above $\Gamma_{25'}$ [16, 17] in order to accommodate the extra electron. The fourth and fifth bands which are completely empty in Nb then become partially filled in Mo, causing the appearance of electron pockets around Γ and other complex changes in the FS topology.

We turn now to the FSs of disordered Nb–Mo alloys with reference to figures 2(b)–2(d) and tables 3–5 [19–27]. The evolution of various FS sheets of Nb upon adding Mo is considered first. Of the three FS sheets of Nb, the N-centred ellipsoid (NCE) hole is observed throughout the composition range. As expected, its size decreases when Mo is added since the average number of electrons per atom increases. The changes in the NCE dimensions are more or less rigid-band like as seen from figures 2(b)–2(d). There is a systematic though small departure from the RBM in that the N-to-Γ radius of the NCE in

Table 3. A comparison of the present KKR-CPA and Nb-based rigid-band-model (RBM) predictions of selected radii of various FS sheets in the 25% Mo alloy. All radii are given as fractions of the ΓH distance in the $Nb_{0.75}Mo_{0.25}$ Brillouin zone. The disorder smearing of the FS radii (defined as the half-width at half-maximum of the spectral density function) is given in round brackets with the KKR-CPA column; the smearing for the RBM is zero.

Sheet	Direction	KKR-CPA	RBM
Γ-centred	Γ to H	0.357 (0.001)	0.370
octahedron	Γ to N	0.040 (0.080)	0.110
(GCO)	Γ to P	0.050 (0.030)	0.125
N-centred	N to Γ	0.288 (0.003)	0.287
ellipsoid	N to H	0.181 (0.003)	0.184
(NCE)	N to P	0.307 (0.003)	0.307
'Jungle-gym'	N to Γ	0.670 (0.080)	0.505
(JGA)	N to H	0.305 (0.002)	0.298
	Γ to P	0.050 (0.030)	0.125
	H to P	0.330 (0.002)	0.330

Table 4. As table 3, except that this table refers to $Nb_{0.50}Mo_{0.50}$. Note that theories 1 and 2 generally yield non-zero FS smearing which we have not attempted to read from the figures in the relevant references for the present illustrative purposes.

Sheet	Direction	Theory 1 [22]	Theory 2 [23]	Theory 3 [27]	KKR-CPA	RBM
Γ-centred	Γ to H	0.18	0.22	0.17	0.199 (0.008)	0.121
octahedron	Γ to N	0.09	0.17	0.12	0.138 (0.006)	0.084
(GCO)	Γ to P	—	—	—	0.126 (0.005)	0.078
H-centred	H to Γ	0.60	0.53	0.60	0.580 (0.008)	0.647
octahedron	H to N	0.38	0.34	0.37	0.370 (0.002)	0.386
(HCO)	H to P	—	—	—	0.310 (0.002)	0.320
N-centred	N to Γ	0.32	0.24	0.25	0.257 (0.003)	0.247
ellipsoid	N to H	0.21	0.15	0.16	0.161 (0.001)	0.163
(NCE)	N to P	—	—	—	0.277 (0.003)	0.273
'Bud'	Diameter along Δ	0.08	0.16	0.08	0.100 (0.010)	<0.02
	Maximum width ⊥ to Δ in (110) plane	0.22	0.12	0.06	0.080 (0.010)	<0.02

the KKR-CPA does not shrink as rapidly as the RBM; for 75% Mo this radius is nearly 10% larger in the KKR-CPA (see table 5).

The behaviour of the Γ-centred octahedron (GCO) and the jungle-gym arm (JGA) of Nb is more complicated. In the 25% Mo alloy, E_F lies just below $\Gamma_{25'}$, so all FSs are still hole like even though both the GCO and the JGA have shrunk; the changes in size and shape are quite non-rigid-band like at and around the Γ point (figure 2(b)). Table 3 shows that while some of the radii of the GCO and JGA sheets are given quite well by the rigid-band model (RBM), others differ greatly between the KKR-CPA and the RBM. In the 50% as well as the 75% Mo alloys, E_F moves above $\Gamma_{25'}$, and the hole-like GCO and JGA sheets become electron like; the alloy FS now resembles that of Mo more than

Table 5. As table 3, except that this table refers to $Nb_{0.25}Mo_{0.75}$.

Sheet	Direction	KKR-CPA	RBM
Γ-centred electron 'jack' (GCE)	Γ to H	0.520 (0.005)	Not formed clearly
	Γ to N	0.211 (0.002)	
	Γ to P	0.192 (0.002)	
H-centred octahedron (HCO)	H to Γ	0.522 (0.005)	0.522
	H to N	0.334 (0.002)	0.351
N-centred ellipsoid (NCE)	N to Γ	0.221 (0.001)	0.199
	N to H	0.133 (0.001)	0.131
	N to P	0.234 (0.002)	0.224
'Lens'	Diameter along Δ	0.030 (0.010)	Not formed clearly
	Maximum width ⊥ to Δ in (110) plane	0.070 (0.010)	Not formed clearly

that of Nb. The RBM describes this change in the FS character qualitatively, but is of little quantitative value in these cases. For example, the radii of the Γ-centred octahedron (GCO) in the 50–50 alloy differ between the KKR-CPA and the RBM by a factor of about 1.5; similarly the 'bud' which is barely visible in the RBM is well formed in the KKR-CPA. In the 75% Mo alloy (figure 2(d)), the 'electron lens' is not formed in the RBM, whereas in the KKR-CPA the 'electron jack' and the 'lens' appear to be formed.

Turning to the question of disorder-induced smearing $\Delta(\boldsymbol{k})$ of the FS, tables 3–5 show that generally the size of smearing is quite small. The absolute values of the disorder smearing are less than 1% of the ΓH zone dimension for most sheets throughout the composition range, consistent with a weak-scattering picture of the electronic structure of the Nb–Mo system. The 25% Mo alloy is seen to be an exception in that the values of $\Delta(\boldsymbol{k})$ in a few cases are as large as 8% of ΓH. This, however, does not represent the failure of the weak-scattering model but is a consequence of the fact that the width $\Delta\boldsymbol{k}$ of a $\boldsymbol{k}$-state is related to the intrinsic width ΔE in energy via the factor $1/|\mathrm{d}E/\mathrm{d}k|$ (see [40] for a discussion). Therefore, even though ΔE is small over much of the energy region around E_F, $\Delta\boldsymbol{k}$ gets magnified when flat bands are involved as is the case in the 25% Mo alloy where E_F lies near $\Gamma_{25'}$. The width $\Delta\boldsymbol{k}$ should be kept in mind in assessing the effects of a given FS sheet in various observable properties of the system in an alloy.

Further insight into the composition dependence of the FS of $Nb_{1-x}Mo_x$ is provided by figure 3 and table 6 which present FS cross sections in the (100) plane ΔDG displaced from the zone centre Γ along k_z by a height equal to a tenth of the ΓH distance, i.e. in an off-centre plane parallel to the (100) plane of figure 2. These results are interesting because they reveal that the dimensions of several FS features are rather small along k_z; for example, we see that the electron lens and the jack of figure 2(d) are absent in the cross section of figure 3(d) for 75% Mo; the sizes of the H- as well as the Γ-centred holes are also substantially smaller in figure 3(d) compared to 2(d). Much of the commentary of the two preceding paragraphs concerning the composition dependence of the sizes and disorder smearings of various FS orbits, as well as similarities of and differences between the KKR-CPA and RBM predictions in connection with figure 2 above, is applicable here with obvious changes and need not be repeated.

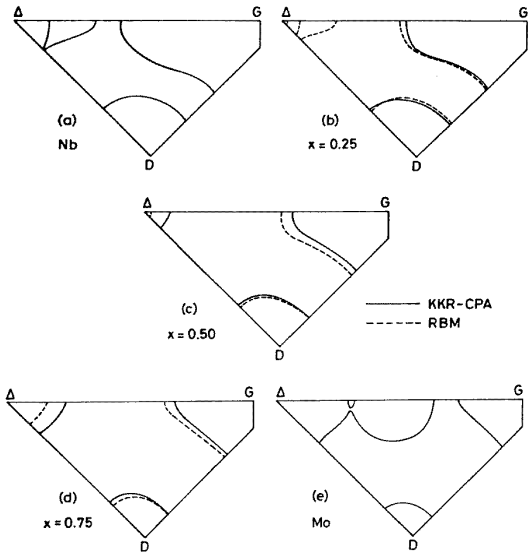

Figure 3. Cross sections of the Fermi surface in the ΔDG plane (parallel to the central (100) plane but displaced through $0.1 \times \Gamma H$ distance; see the text): (a) Nb, (b) $Nb_{0.75}Mo_{0.25}$, (c) $Nb_{0.50}Mo_{0.50}$, (d) $Nb_{0.25}Mo_{0.75}$, and (e) Mo. The dashed lines indicate the RBM results. The Δ point lies vertically above Γ, D above N, and G in a ΓNH plane.

Table 6. As table 3, except that this table compares KKR-CPA and RBM radii in the ΔDG symmetry plane for various compositions x in $Nb_{1-x}Mo_x$; see also figure 3.

Direction	x	KKR-CPA	RBM
Δ to D	0.0	0.138, 0.451	—
	0.25	0.015 (0.030)	0.071, 0.096
		0.464 (0.003)	0.467
	0.50	0.085 (0.006)	0.025
		0.488 (0.002)	0.498
	0.75	0.164 (0.003)	0.120
		0.523 (0.002)	0.543
	1.0	0.217, 0.558	—
Δ to G	0.0	0.121, 0.297, 0.393	—
	0.25	0.013 (0.060)	0.062, 0.203
		0.462 (0.007)	0.436
	0.50	0.095 (0.008)	0.026
		0.538 (0.004)	0.503
	0.75	0.206 (0.005)	0.142
		0.608 (0.003)	0.577
	1.0	0.271, 0.285	—
		0.572, 0.662	—

Although in much of the discussion so far we have compared and contrasted our KKR-CPA with the corresponding RBM predictions, some intercomparisons with other theoretical results in the literature are appropriate. In this connection, three different sets of theoretical columns are appended in table 4 for the 50–50 alloy; scattered results at other compositions could be adduced from the literature but the data of table 4 are adequate for illustrative

purposes. The VCA (theory 3) is seen to be in better accord with our KKR-CPA than the RBM. This is expected since the VCA incorporates the changes in the average crystal potential upon alloying; note, however, that the VCA incorrectly yields a strictly vanishing disorder smearing of states. Interestingly, the ATA (theory 2) radii are not on the whole in better accord with the KKR-CPA than the VCA. In fact, the non-charge-self-consistent CPA (theory 1) radii differ rather substantially from our charge self-consistent results; for example, in theory 1, the size of the N-centred ellipsoid is about 25% larger, and the maximum width of the 'bud' (the last row of table 4) is nearly three times larger. The aforementioned differences between various theoretical results highlight the difficulties endemic to non-self-consistent calculations.

Concerning comparison with experiment, most relevant are [26] and [27] which report a high-statistics 2D-ACAR positron annihilation study of the FS of a 50–50 Nb–Mo single crystal. In [26] and [27] it is deduced that the size of the N-centred ellipsoid in the 50–50 alloy is well described by the VCA; given the good agreement between our KKR-CPA and the VCA (theory 3 in table 4), it follows that the experimental results of [26, 27] are in accord with the present KKR-CPA predictions. (The relatively small differences between KKR-CPA and VCA in table 4 would not be resolvable in this experiment.) Incidentally, the previous non-self-consistent KKR-CPA calculations (theory 1) yield FS dimensions for this sheet substantially larger than the experimental results.

While the behaviour of the N-centred ellipsoid is thus satisfactorily understood, the experimental situation with regard to other FS sheets is unclear; the obscuring effects of the projection [41, 42] involved in the measurements of [26, 27] made it difficult to deduce the radii of other FS sheets. This is unfortunate since it is the composition dependence of the Γ-centred sheets which would provide the most discriminating test of the KKR-CPA model. Notably, in [24] a 25% Mo sample was studied via the 2D-ACAR technique, and the results, though qualitative, hint at possible deviations from the RBM near the Γ point; see figure 7 of [24].

The measurement of fine features of the FS topology of $Nb_{1-x}Mo_x$, such as the Γ-centred sheets, will present a challenge to the 2D-ACAR technique; note that experiments such as the dHvA ones which require long electron mean free paths are not suited for the investigation of concentrated alloys. In this connection, recent work aimed at 3D reconstruction of the occupation number density, $n(\boldsymbol{k})$, in metals and alloys appears promising. For example, in [5] a 3D rendition of the FS of $Li_{1-x}Mg_x$ alloys was obtained throughout the composition range, although in this case the FS is relatively simple as it consists of a single free-electron-like sheet. In [43] a 3D determination of the FS of Nb using image reconstruction techniques [43–45] was reported; it was based on the Fourier transform methods, including cross sections of the FS in several planes parallel to the (100) plane passing through the zone centre. In [46] the three-dimensional second- and third-band FS of V were reconstructed from the measured 2D-ACAR data [47, 48], as also were the cross sections of the jungle-gym arm at different distances from Γ along ΓH. A study of the FS of $Nb_{1-x}Mo_x$ along these lines [43–48] should prove interesting.

Figure 2 shows that FS sheets, such as the jungle-gym arms in Nb and the H- and Γ-centred sheets in Mo, are flat in some momentum regions (marked as P_1 and P_2). Electronic transitions across such flat sheets can give rise to Kohn anomalies in phonon dispersion curves [14] or drive concentration waves in disordered alloys [49]. The present work gives some insight into the Kohn anomalies in Nb, Mo, and Nb–Mo alloys reported by Powell *et al* [14]. In Nb the Kohn anomaly was observed in the Λ_1 branch at the reduced wave-vector $\zeta = 0.46$, and ascribed to transitions across the jungle-gym arms through H (see figure 11 in [14]); the relevant theoretical distance is P_1H in figure 2(a) which is 0.35 of the ΓH

length, and yields $\zeta = 0.40$, in reasonable agreement with experiment. A similar analysis of figure 2(b) gives the theoretical value of $\zeta = 0.38$ for $Nb_{0.75}Mo_{0.25}$, consistent with the experimental finding that the anomaly moves to smaller values of ζ with increasing x; it is difficult to deduce quantitative values of ζ in alloys experimentally because disorder scattering of states tends to wash out the anomalies. Finally, we note that for Mo figure 2(e) suggests three Kohn anomalies at ζ-values of 0.30, 0.71, and 0.99 along the [111] direction (related to distances ab, ed, cd in figure 11 of [14]); these are in good accord with the corresponding experimental values of $\zeta = 0.27$, 0.78, and 0.96 of [14].

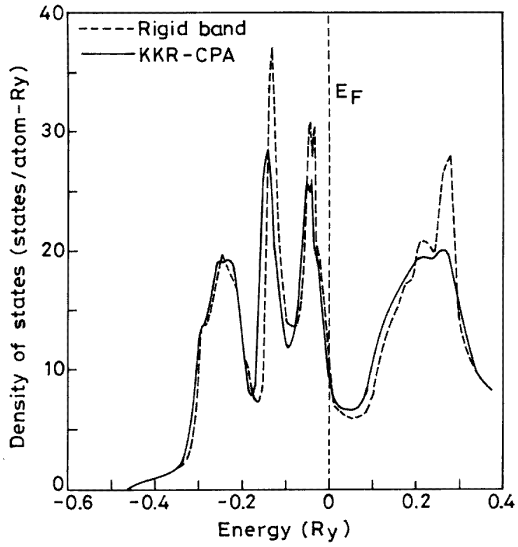

Figure 4. KKR-CPA and RBM densities of states for $Nb_{0.50}Mo_{0.50}$.

3.2. The density of states

We note first that our results for the DOSs for Nb and Mo are in good accord with earlier KKR calculations of [50], and the LCGO computations of [16, 17]. In Nb–Mo alloys also our densities of states as well as the site-decomposed densities of states are more or less similar to the various published results [18, 19], some differences notwithstanding. Here we give an overview of the salient features of the electronic spectrum with the help of figures 4–7 (see [51] for details).

Figure 4 shows that although the KKR-CPA and the Nb-based rigid-band DOS are quite similar for energies $E \leqslant E_F$, they are less so for $E > E_F$. In this regard, the results of figure 4 for the 50–50 alloy are typical of other compositions. This is to be expected in view of figure 5 which shows that the Nb- and Mo-site-resolved component densities of states differ mainly in the region where $E > E_F$ for all alloy compositions. Figure 6 which shows the l-decomposed densities for the 50–50 alloy further indicates that the difference between the Nb and Mo sites is localized in the e_g channel, the contributions of the s, p, and t_{2g} components being quite similar throughout the energy range. In comparing the KKR-CPA and the RBM we should keep in mind that the KKR-CPA DOS will generally be smoother due to the presence of disorder scattering of states which is implicitly neglected in the RBM. Incidentally, our DOS in Nb–Mo is closer to that of [19] than that of [18];

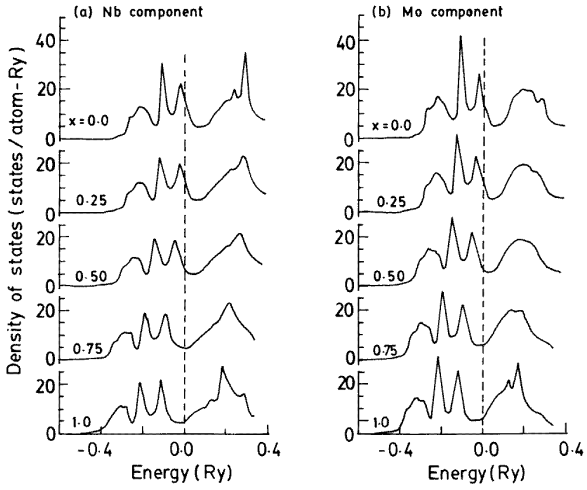

Figure 5. (a) Nb- and (b) Mo-component KKR-CPA DOSs in $Nb_{1-x}Mo_x$ for various values of the concentration x.

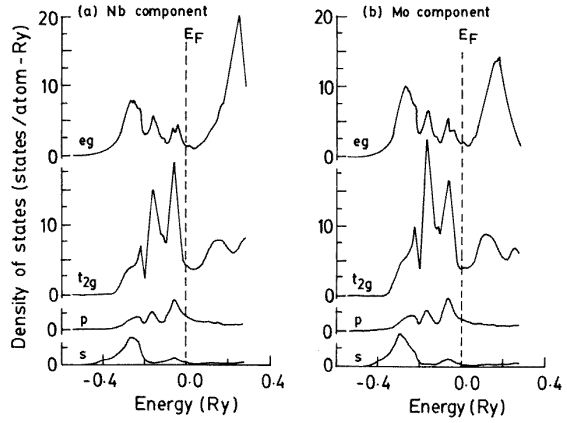

Figure 6. *l*-decompositions of (a) Nb- and (b) Mo-component KKR-CPA DOSs in $Nb_{0.5}Mo_{0.5}$.

recall that the computations of both [19] and [18] are non-charge-self-consistent, and differ from each other due to differences in the input crystal potential.

Figure 7(a) shows that our computed DOS at $E = E_F$ ($\rho(E_F)$) for $Nb_{1-x}Mo_x$ is in reasonable accord with the values obtained by McMillan [11] from an analysis of the specific heat data; the discrepancy for pure Nb is not serious because E_F in this case lies rather close to a peak in the DOS; see figure 5(a). The addition of Mo causes E_F to move away from the DOS peak in Nb which is the main reason for the rapid decrease in the DOS in figure 7(a) for Mo concentration $x \leqslant 0.5$. Figure 7(b) provides further insight into the character of states responsible for this rapid variation in the DOS in Nb-rich alloys; we see that this decrease is mostly in the t_{2g} part (open circles in figure 7(b)) of the Nb-component DOS. The e_g part on both Nb and Mo sites is quite flat, and the s and p components (not shown) are small and slowly varying with composition.

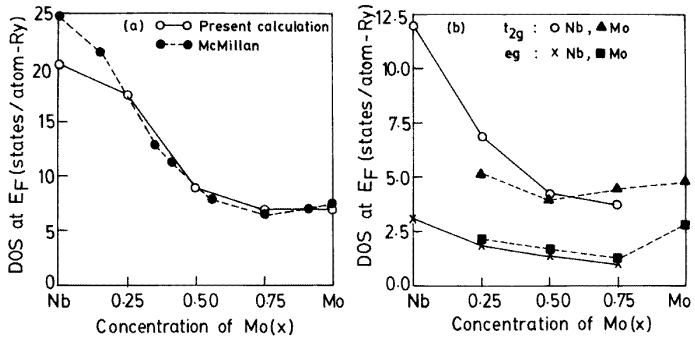

Figure 7. (a) The variation of the KKR-CPA DOS at E_F with Mo concentration. (b) t_{2g} and e_g parts of the Nb- and Mo-component DOSs. Points have been joined by straight lines to guide the eye.

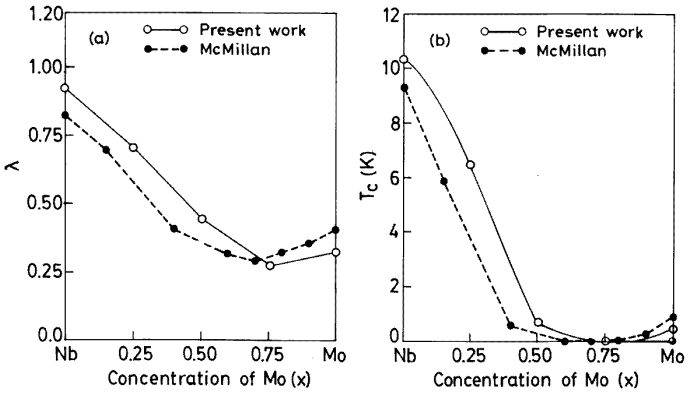

Figure 8. (a) The electron–phonon coupling constant λ, and (b) T_c for $Nb_{1-x}Mo_x$ as functions of x. Points have been joined by straight lines to guide the eye.

Table 7. Values of McMillan–Hopfield parameters η, electron–phonon coupling coefficients λ, the effective Coulomb repulsion μ^*, and superconducting temperatures T_c from KKR-CPA calculations for $Nb_{1-x}Mo_x$.

x_{Mo}	η_{Nb} (eV Å^{-2})	η_{Mo} (eV Å^{-2})	λ	μ^*	T_c (K)
0.00	8.140	5.970	0.926	0.153	10.257
0.25	7.208	5.514	0.699	0.134	6.516
0.50	4.116	3.539	0.342	0.093	0.619
0.75	3.563	3.840	0.276	0.088	0.147
1.00	3.762	5.369	0.326	0.098	0.418

3.3. The electron–phonon coupling constant λ and the superconducting transition temperature T_c

We now discuss our theoretical results with reference to figure 8 and tables 7 and 8. Figure 8(a) shows that the composition dependence of λ in Nb–Mo alloys computed via equation (3) is similar to that deduced empirically by McMillan [11], although the KKR-CPA

Table 8. Contributions to McMillan–Hopfield parameters η (eV Å^{-2}) from $(l, l+1)$-channels.

x_{Mo}	η^{Nb}_{s-p}	η^{Nb}_{p-d}	η^{Nb}_{d-f}	η^{Nb}_{tot}	η^{Mo}_{s-p}	η^{Mo}_{p-d}	η^{Mo}_{d-f}	η^{Mo}_{tot}
0.00	0.364	3.014	4.762	8.140	0.218	1.539	4.213	5.970
0.25	0.316	2.694	4.199	7.208	0.194	1.451	3.869	5.514
0.50	0.335	1.655	2.126	4.116	0.214	1.048	2.277	3.539
0.75	0.199	1.223	2.141	3.563	0.126	0.937	2.776	3.840
1.00	0.083	0.898	2.781	3.762	0.058	0.883	4.427	5.369

value is higher in Nb and lower in Mo; here, following [11], we have used $\langle\omega^2\rangle^{1/2}_{Nb} = 230$ K, and $\langle\omega^2\rangle^{1/2}_{Mo} = 310$ K in equation (3), together with the KKR-CPA values of η_{Nb} and η_{Mo} listed in table 7. The T_c computed via equations (1) and (2) is seen from figure 8(b) to display a variation with Mo content similar to the experimental data; the Debye temperatures which enter equation (1) were taken for $Nb_{1-x}Mo_x$, as $\Theta_D = 277.0$ K, 307.4 K, 400.0 K, 451.5 K, and 460.0 K for $x = 0.00$, 0.25, 0.50, 0.75 and 1.00, respectively [11]. The discrepancy in the absolute value of T_c between theory and experiment could be removed by invoking a higher value of μ^* following [8]. On the whole, these results suggest that the KKR-CPA theory in conjunction with equations (1)–(4) may constitute a simple reasonable scheme for predicting the composition dependence of T_c for disordered alloys more generally.

It should be noted that although we have used the values of $\langle\omega^2\rangle^{1/2}_{Nb} = 230$ K and $\langle\omega^2\rangle^{1/2}_{Mo} = 310$ K given by [11], there is no consensus in the literature with regard to this choice. In [31] $\langle\omega^2\rangle^{1/2}_{Nb} = 183$ K and $\langle\omega^2\rangle^{1/2}_{Mo} = 251$ K are suggested. On the other hand [13] invokes $\langle\omega^2\rangle = \frac{1}{2}\Theta^2_D$ which yields a T_c of about 16 K in Nb, prompting the authors to argue that the RMTA overestimates the η_{df}-contribution to λ, which should be reduced by a factor of 2. However, more recently in [8] a first-principles estimation of λ in Nb was obtained using linear response theory, but it was concluded that the culprit is not the RMTA but that the parameter μ^* should be higher than the McMillan value of 0.13. These remarks should make it clear that our use of equations (1)–(4) with the stated values of various parameters is by no means unique, and that the situation in this regard is far from clear in the literature.

Finally, we comment briefly on the changes in η_{Nb} and η_{Mo} in $Nb_{1-x}Mo_x$ as functions of x given in table 8. The maximum contribution in each case is seen to arise through the d–f channel as expected. Both η_{Nb} and η_{Mo} decrease with increasing x, although the values increase in the Mo limit. This trend correlates with the behaviour of the DOS $\rho(E_F)$ at the Fermi energy which is involved in the definition of η (equation (4)). Also η on the Nb as well as the Mo site falls rapidly in the Nb-rich region until $x = 0.5$, and then rather slowly becomes nearly flat at the Mo-rich end, much like T_c.

4. Conclusions and discussion

We have carried out a systematic study of the electronic structure and superconducting properties of $Nb_{1-x}Mo_x$ alloys over the entire bcc solid solution range using the all-electron fully charge-self-consistent KKR-CPA methodology. The composition dependences of the Fermi surface (FS), the density of states (DOS), and the transition temperature (T_c), and the associated parameters (λs and ηs) are discussed. Extensive comparisons with the Nb-based rigid-band model as well as other available theoretical results are made, and effects of alloying beyond the simple band filling associated with the addition of an electron in

going from Nb to Mo are delineated. Concerning the FSs, while the N- and H-centred hole sheets of Nb shrink essentially rigidly, the Γ-centred sheets do not; the latter sheets evolve in a highly non-rigid-band manner causing complex changes in the FS topology of Nb with increasing Mo content. The 25% Mo alloy displays an especially large disorder-induced smearing of the Γ-centred FS sheets. Direct experimental information concerning FS dimensions is available only for the N-centred ellipsoids via positron annihilation measurements which are in accord with our results. In examining the DOSs, we find that the DOSs for $E < E_F$ vary more rigidly than those for $E > E_F$, and that the differences between the Nb- and Mo-site-decomposed DOSs are localized mainly in the e_g channel. In connection with the superconductivity of $Nb_{1-x}Mo_x$, η and λ are found to decrease rapidly for $x < 0.5$ and relatively slowly thereafter. Using the computed λs, the x-dependence of T_c is described reasonably well in a simple scheme which invokes the McMillan formula [11] for T_c and the Bennemann–Garland [29] expression for μ^*. We suggest that such an approach may be useful more generally for treating T_cs in disordered alloys within the KKR-CPA framework. It is hoped that our work which presents unique predictions of the local density KKR-CPA-type theory will encourage further experimental studies on $Nb_{1-x}Mo_x$, especially of the evolution of the Γ-centred FS sheets, and of the composition dependence of λ in the Nb-rich alloys.

Acknowledgments

One of us (RP) thanks for hospitality the International Centre for Theoretical Physics, Trieste, where part of this work was carried out. It is a pleasure for AB to acknowledge the hospitality of CSIR and UNDP under the TOKTEN scheme which enabled this study to be completed. This research was supported by the Department of Science and Technology, New Delhi, India, through Grant SP/S2/M-39/87, the USDOE Contract W-31-109-ENG-38 including a subcontract to Northeastern University, and benefited from a travel grant from NATO, and the allocation of time at NERSC and PSC supercomputer centres.

References

[1] Bansil A 1987 *Electronic Band Structure and its Applications* ed M Yussouff (Berlin: Springer) p 273; 1993 *Z. Naturf.* a **48** 165
Bansil A, Kaprzyk S and Tabola A 1992 *Mater. Res. Soc. Symp. Proc.* **253** 505
[2] Stocks G M and Winter H 1984 *The Electronic Structure of Complex Systems* ed P Phariseau and W M Temmerman (New York: Plenum) p 463
[3] Bansil A and Kaprzyk S 1991 *Phys. Rev.* B **43** 10 335
Kaprzyk S and Bansil A 1990 *Phys. Rev.* B **42** 7358
[4] Prasad R 1995 *Methods of Electronic Structure Calculations* ed O K Andersen, V Kumar and A Mookerjee (Singapore: World-Scientific) p 211; 1991 *Indian J. Pure Appl. Phys.* **29** 255
[5] Rajput S S, Prasad R, Singru R M, Trifthauser W, Eckert A, Kogel G, Kaprzyk S and Bansil A 1993 *J. Phys.: Condens. Matter* **5** 6419
[6] Elliot R P 1965 *Constitution of Binary Alloys* 1st suppl. (New York: McGraw-Hill) p 260
[7] Butler W H, Smith H G and Wakabayashi N 1977 *Phys. Rev. Lett.* **39** 1004
Butler W H, Pinski F J and Allen P B 1979 *Phys. Rev.* B **19** 3708
[8] Savrasov S Y, Savrasov D Y and Andersen O K 1994 *Phys. Rev. Lett.* **72** 372
[9] Crabtree G W, Dye D H, Karim D P, Koelling D D and Ketterson J B 1979 *Phys. Rev. Lett.* **42** 390
[10] Bostock J, MacVicar M L A, Arnold G B, Zasadzinski J and Wolf E L 1980 *Superconductivity in d- and f-band Metals* ed H Suhl and M B Maple (New York: Academic) p 153
[11] McMillan W L 1968 *Phys. Rev.* **167** 331
[12] Pickett W E and Allen P B 1974 *Phys. Lett.* **48A** 91; 1975 *Phys. Rev.* B **11** 3599

[13] Papaconstantopoulos D A, Boyer L L, Klein B M, Williams A R, Moruzzi V L and Janak J F 1977 *Phys. Rev.* B **15** 4221
[14] Powell B M, Martel P and Woods A D B 1968 *Phys. Rev.* **171** 727
[15] Weber W 1973 *Phys. Rev.* B **8** 5093
[16] Jani A R, Brener N E and Callaway J 1988 *Phys. Rev.* B **38** 9425
[17] Jani A R, Tripathi G S, Brener N E and Callaway J 1989 *Phys. Rev.* B **40** 1593
[18] Giuliano E S, Ruggeri R, Gyorffy B L and Stocks G M 1978 *Transition Metals (Toronto, 1977)* ed M J G Lee, J M Perz and E Fawcett (Bristol: Institute of Physics Publishing) p 410
[19] Donato E, Giuliano E S, Ruggeri R and Stancanelli A 1979 *Phys. Status Solidi* b **95** K37
[20] Colavita E, Franciosi A, Rosei R, Sacchetti F, Giuliano E S, Ruggeri R and Lynch D W 1979 *Phys. Rev.* B **20** 4864
[21] Giuliano E S, Ruggeri R, Donato E and Stancanelli A 1981 *Nuovo Cimento* **66** 118
[22] Donato E, Ginatempo B, Giuliano E S, Ruggeri R and Stancanelli A 1982 *Phys. Status Solidi* b **110** 39
[23] Nakao Y and Wakoh S 1982 *J. Phys. Soc. Japan* **49** 2423; 1982 *J. Phys. Soc. Japan* **51** 2840, 2847; 1983 *J. Phys. Soc. Japan* **52** 3122
[24] Manuel A A, Oberli L, Jarlborg T, Sachot R, Descouts P and Peter M 1982 *Positron Annihilation* ed P G Coleman, S C Sharma and L M Diana (Amsterdam: North-Holland) p 281
[25] Shiotani N, Okada T, Sekizawa H and Nakamichi T 1983 *J. Phys. Soc. Japan* **52** 2858
[26] Bull C R, Walker J H, Alam A, Shiotani N and West R N 1984 *Phys. Rev.* B **29** 6378
[27] Kaiser J H, Walters P A, Bull C R, Alam A, West R N and Shiotani N 1987 *J. Phys. F: Met. Phys.* **17** 1243
[28] Bujard P, Sanjines R, Walker E, Ashkenazi J and Peter M 1981 *J. Phys. F: Met. Phys.* **11** 775
de Camargo P C, Brotzen F R and Steinemann S 1987 *J. Phys. F: Met. Phys.* **17** 1065
[29] Bennemann K H and Garland J W 1972 *AIP Conf. Proc.* **4** 103
[30] von Barth U and Hedin L 1972 *J. Phys. C: Solid State Phys.* **5** 1629
[31] Allen P B and Dynes B C 1973 *Phys. Rev.* B **12** 905
[32] Pictet O, Jarlborg T and Peter M 1987 *J. Phys. F: Met. Phys.* **17** 221
[33] Gyorffy B L 1976 *Superconductivity in d- and f-band Metals* ed D H Douglass (New York: Plenum) p 29
[34] Gaspari G D and Gyorffy B L 1972 *Phys. Rev. Lett.* **28** 801
[35] Karim D P, Ketterson J B and Crabtree G W 1978 *J. Low. Temp. Phys.* **30** 389
[36] Wakoh S, Kubo Y and Yamashita J 1975 *J. Phys. Soc. Japan* **38** 416
[37] Ketterson J B, Koelling D D, Shaw J C and Windmiller L R 1975 *Phys. Rev.* B **11** 1447
[38] Cleveland J R and Stanford J L 1971 *Phys. Rev.* B **4** 311
[39] Shiotani N, Okada T, Sekizawa H, Wakoh S and Kubo Y 1977 *J. Phys. Soc. Japan* **43** 1229
[40] Prasad R, Papadopoulos S C and Bansil A 1980 *Phys. Rev.* B **21** 496
[41] Lock D G, Crisp V H C and West R N 1973 *J. Phys. F: Met. Phys.* **3** 561
[42] Wakoh S and Matsumoto M 1990 *J. Phys.: Condens. Matter* **2** 797
[43] Kubota T, Kondo H, Watanabe K, Murakami Y, Cho Y K, Tanigawa S, Kawano T and Bahng G W 1990 *J. Phys. Soc. Japan* **59** 4494
[44] Suzuki R, Osawa M, Tanigawa S, Matsumoto M and Shiotani N 1989 *J. Phys. Soc. Japan* **58** 3251
[45] Kubota T, Nakashima H, Murakami Y, Kondo H and Tanigawa S 1992 *Mater. Sci. Forum* **105–110** 727
[46] Pecora L M 1989 *J. Phys.: Condens. Matter* **1** SA1
[47] Singh A K, Manuel A A, Singru R M, Sachot R, Walkers E, Descouts P and Peter M 1985 *J. Phys. F: Met. Phys.* **15** 2375
[48] Pecora L M, Ehrlich A C, Manuel A A, Singh A K, Peter M and Singru R M 1988 *Phys. Rev.* B **37** 6772
[49] Gyorffy B L and Stocks G M 1983 *Phys. Rev. Lett.* **50** 374
[50] Moruzzi V L, Janak J F and Williams A R 1978 *Calculated Electronic Properties of Metals* (New York: Pergamon)
[51] Rajput S S 1990 *PhD Thesis* Indian Institute of Technology, Kanpur